



New depowdering-friendly designs for three-dimensional printing of calcium phosphate bone substitutes



A. Butscher^{a,b,*}, M. Böhner^a, N. Doebelin^a, S. Hofmann^b, R. Müller^b

^aRMS Foundation, Bischmattstrasse 12, CH-2544 Bettlach, Switzerland

^bInstitute for Biomechanics, ETH Zurich, Wolfgang-Pauli-Strasse 10, CH-8093 Zurich, Switzerland

ARTICLE INFO

Article history:

Received 8 April 2013

Received in revised form 19 June 2013

Accepted 16 July 2013

Available online 24 July 2013

Keywords:

Three-dimensional printing (3DP)

Calcium phosphates (CaP)

Ceramic powder

Synthetic bone substitute

Scaffold

ABSTRACT

Powder-based three-dimensional printing (3DP) is a versatile method that allows creating synthetic calcium phosphate (CaP) scaffolds of complex shapes and structures. However, one major drawback is the difficulty of removing all remnants of loose powder from the printed scaffolds, the so-called depowdering step. In this study, a new design approach was proposed to solve this problem. Specifically, the design of the printed scaffolds consisted of a cage with windows large enough to enable depowdering while still trapping loose fillers placed inside the cage. To demonstrate the potential of this new approach, two filler geometries were used: sandglass and cheese segment. The distance between the fillers was varied and they were either glued to the cage or free to move after successful depowdering. Depowdering efficiency was quantified by microstructural morphometry. The results showed that the use of mobile fillers significantly improved depowdering. Based on this study, large 3DP scaffolds can be realized, which might be a step towards a broader clinical use of 3D printed CaP scaffolds.

© 2013 Acta Materialia Inc. Published by Elsevier Ltd. All rights reserved.

1. Introduction

Powder-based three-dimensional printing (3DP) is a versatile method to produce synthetic scaffolds and bone graft substitutes. It allows an outstanding flexibility in geometry and material [1]. Freedom in choice of materials also allows the use of calcium phosphate (CaP) biomaterials [2–7]. Furthermore 3DP provides geometrical flexibility for virtually unlimited shapes and structures, at least from a theoretical point of view. Due to the absence of typical constraints of traditional production methods, any geometry that contains features within the range of 3DP resolution is feasible. In theory, these great advantages make powder-based 3DP perfectly suitable for building up complex shaped scaffolds and bone graft substitutes. This is especially appealing, as biocompatibility of 3DP scaffolds has already been demonstrated by successful *in vivo* applications [8–11].

However, considering the literature, it is obvious that in practice the scaffolds produced by powder-based 3DP do not reflect the great geometrical flexibility of this method. Typically 3DP is used to produce rather simple and small objects such as cubes and cylinders with a rather simple and regular inner architecture [8,10,12–18]. Even in the case of more complex structures, e.g.

custom-made 3DP models, the inner structures of such structures are predominantly isotropic and typically limited to simple cylindrical bores in a homogeneous body [19,20].

In our previous work, a moisture-based 3DP method was proposed to enhance the accuracy of the method [21]. Moisture was used to stabilize the powder bed just before printing and thus improve 3DP accuracy. The accuracy was quantified by looking at outer dimensions of simple solid bodies and roughness values on the outside of a printed pyramid structure. However, the critical inside part of the printed porous objects was neglected. In 3DP, the solid is created by the reaction of a liquid selectively sprayed onto a powder bed. After printing, the hardened object is embedded in the powder bed and all non-hardened areas, including pores and cavities, are filled with loose powder. Once the printed object is cleared from the surrounding powder in the build volume of the printer, the final and most critical step of powder clearance is still to come, where the loose powder within the printed object's pores and cavities must be removed. If this critical step, also referred to as depowdering, cannot be accomplished, the printed porous object is of no use.

To our knowledge, depowdering of 3DPCaP scaffolds has not been studied and published in depth yet. Depowdering is particularly difficult when the pores and pore interconnections are small and/or when the object is large. As a result, 3D printed porous objects are limited to small dimensions and large pores. Furthermore the 3DP resolution is limited. For example, it has been

* Corresponding author at: RMS Foundation, Bischmattstrasse 12, CH-2544 Bettlach, Switzerland. Tel.: +41 32 644 1400; fax: +41 32 644 1176.

E-mail address: Andre.Butscher@rms-foundation.ch (A. Butscher).

reported that macropores smaller than 500 μm currently cannot be achieved using 3DP [1]. Even though it is still unclear what the optimal pore size for vascularization and cell proliferation is [22], most authors agree that an adequate range should probably be between 50 and 1000 μm [6,23,24]. Considering this conflicting requirement, there is a clear need for new approaches within powder-based 3DP. Especially the need for large scaffolds and at the same time a pore size and porosity range not only controllable at the periphery but especially in the middle of the scaffold is a challenging task.

Therefore, the present study aims at improving the depowdering step by exploiting 3DP versatility. Specifically, scaffolds consisting of two distinct parts are printed at once: the outer part consists of a stiff but porous CaP cage whose windows are large enough to enable depowdering while still trapping the inner part consisting of loose fillers.

2. Material and methods

2.1. Powder

The printing experiments were performed with a custom-made α -TCP (α -tricalcium phosphate, α - $\text{Ca}_3(\text{PO}_4)_2$) powder. This powder was produced according to a published procedure [25]. In summary, a 0.45:1 M blend of calcium carbonate (CaCO_3 , Merck, Germany, catalogue No. 102076) and monetite (GFS Chemical, USA, catalogue No. 1548) powder was mixed and calcined at 900 °C (Nabertherm, Germany). After sieving (AS 200, Retsch, Switzerland) the calcined powder was sintered at 1400 °C and quenched in air. This sintered powder was finally milled and sieved to get the desired particle range used in this study. The phase composition obtained by this procedure was >95 wt.% α -TCP, as verified by powder X-ray diffraction (XRD). The properties of this powder have been published previously [21]. For the given powder a particle size distribution of $d_{10} = 9 \mu\text{m}$; $d_{50} = 21 \mu\text{m}$; $d_{90} = 37 \mu\text{m}$, specific surface area of $0.28 \text{ m}^2 \text{ g}^{-1}$, a bulk density of 974 kg m^{-3} , a tapped density of 1399 kg m^{-3} and finally a flowability *ffc* (flow factor) of 5.3 was found.

After every printing cycle the unreacted powder was dried in a preheated oven at a temperature of 200 °C for 1 h. It was then sieved with a jet sieving device and a cyclone (e200 LS, Alpine, Germany) and the fraction of particles smaller than 45 μm was reused for further printing. The legitimation of powder recycling was given in detail in our previous work [21]. Our previous study has indeed revealed that the recycled powder did not deteriorate in terms of printing characteristics compared to the original α -TCP powder.

2.2. 3D printer and printed specimens

All samples were printed using a commercial but customized 3D printer (ZPrinter 310 Plus, ZCorporation, USA) as described previously [1]. A constant layer thickness of 50 μm was used for all experiments. A custom-made moisture unit was used to apply 5 s of moisture from a water nebulizer (USV 3002, Schulte, Germany) on every layer in order to stabilize the powder bed via liquid bridges [21] just before printing. In 3DP, the solid is created by the reaction of a liquid selectively sprayed onto this powder bed. In our case, 10 wt.% phosphoric acid solution (Carl Roth, Germany) was used as reaction liquid [14,26]. Phosphoric acid partially dissolved α -TCP powder particles, and these two compounds precipitated locally, resulting in calcium phosphate (CaP) phases of brushite (DCPD, $\text{CaHPO}_4 \cdot 2\text{H}_2\text{O}$) and monetite (DCP, CaHPO_4), known for their excellent *in vivo* behavior [27–31]. Although different definitions for the term “binder” exist, in this paper we refer to

the phosphoric acid solution as “binder”. The local dissolution of powder particles and precipitation of new crystals resulted in an entanglement and thus local binding between previously unbound particles occurred.

Original silicon tubes were replaced by chemically inert PTFE tubes in order to reduce any material degradation due to the use of phosphoric acid in the 3D printer. Furthermore the original polymeric fluid container was replaced by an inert glass container.

Prior to the present study, a systematic analysis of printer settings had been performed with the aim of defining the most adequate binder/volume ratios (defined as saturation). Values of 45% for the shell and 90% for the core saturation were defined. The optimization was done by printing benchmark samples with concavities (Fig. S1) and different potential bone filler designs with convexities (Fig. S2). The printed samples were analyzed macroscopically using imaging software (Image Access 11 Premium, Release 11.3, Imagic, Switzerland).

Various scaffold designs were printed to assess the ability of the new design parameters proposed in this study to improve depowdering. The new design consisted of a cylindrical cage filled with various connected or loose fillers (Fig. 1). The walls included windows with a width of 2 mm preventing the fillers from escaping but allowing the removal of loose powder. The scaffolds varied according to the following parameters: (i) two different shapes of filling objects, namely sandglass (SG, Fig. 1a–c) structures and cheese segments (CS, Fig. 1d–f); (ii) different filler distances, i.e. far, near and glued; and (iii) mechanical properties after post-hardening regimes in 10% phosphoric acid compared to no post-hardening. Filler distances of 0.25/0.5 and 0.5/1 mm for near/far distance were tested for SG and CS fillers, respectively. A summary of experiments and definition of nomenclature can be found in Table 1.

The rationale for the design of the fillers was based on three criteria. First, the fillers had to have a certain printing stability. In other words, the filler geometry had to be chosen such that lateral or rotational motions were minimized during printing. Fillers presenting a flat and large base (e.g. SG and CS) were preferred to spherical designs due to their inherent stability [21]. Second, since osteoinduction is predominantly found in concavities [32], preference was given to filler designs resulting in multiple concavities between their neighbors after depowdering, e.g. SG. Finally, large empty spaces are generally considered to favor soft tissue ingrowth. So the CS geometry was chosen to fill out most of the inner volume.

All specimens were drawn with the CAD software NX 7.5 (PLM Software, Siemens, Germany) and imported into the 3D printing software in the STL (stereolithography) file format.

2.3. 3DP sample characterization

2.3.1. X-ray diffraction

The crystalline composition of pre-printed powders, as well as pre- and post-hardened printed objects, was determined by XRD. XRD was performed using a powder diffractometer (CubiX³, PANalytical, Netherlands) with graphite-monochromated $\text{CuK}\alpha$ radiation in the range 4–60° 2θ . The quantitative phase composition was determined by Rietveld refinement using the software BGMN (<http://www.bgm.de>) version 4.2.20 [33]. Structural models were taken from Mathew et al. [34] for α -TCP, from Dickens et al. [35] for monetite, and from Curry and Jones [36] for brushite. No other phases were identified in the diffraction patterns.

2.3.2. Mechanical testing

The compression strength and diametral tensile strength of printed bulk cylinders were determined before and after post-hardening. Four cylinders were tested for every group using a static

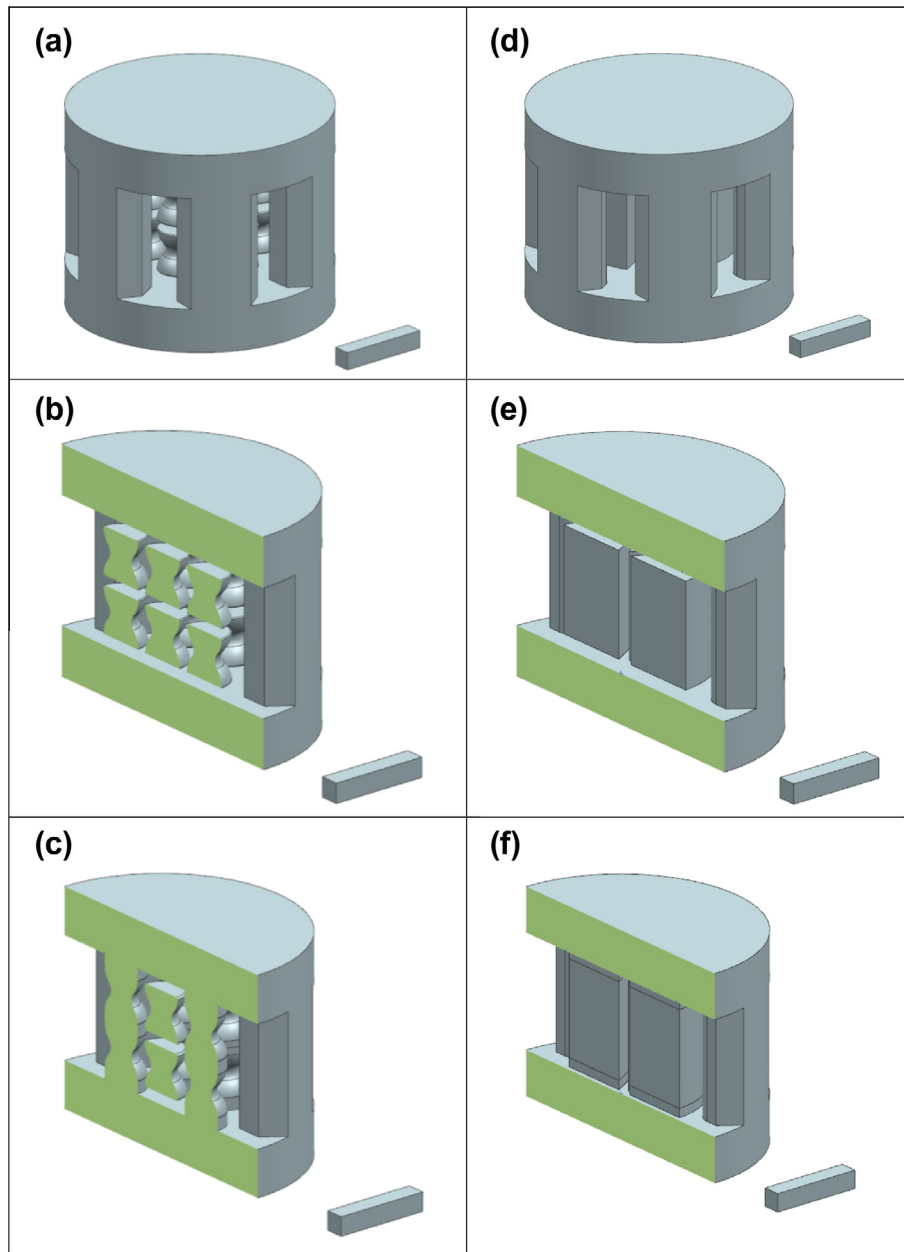


Fig. 1. Overview of different sandglass (SG, a–c) and cheese segment (CS, d–f) scaffolds. Images (a, b, d and e) depict models with free fillers. For comparison purposes, scaffolds with glued fillers (c and f) were included in this study. While for CS all fillers were glued to the cage (f) for SG the fillers in the very center were not glued to enhance the chance of depowdering (c). The bar corresponds to a length of 5 mm.

Table 1

List of experiments, definition of nomenclature for distance between fillers (factor A; low/high distance), filler design (factor B; free vs. glued) and filler type (factor C; SG: sandglass vs. CS: cheese segment) and outer dimensions of scaffolds.

No.	Name	Fillers SG/CS	Design free/glued	Distance low/high	Distance (mm)	Height (mm)	Diameter (mm)
1	SGfl	SG	Free	Low	0.25	11.4	14
2	SGfh	SG	Free	High	0.50	11.4	14.5
3	SGgl	SG	Glued	Low	0.25	11.4	14
4	SGgh	SG	Glued	High	0.50	11.4	14.5
5	CSfl	CS	Free	Low	0.50	11.4	15
6	CSfh	CS	Free	High	1.00	11.4	15
7	CSgl	CS	Glued	Low	0.50	11.4	15
8	CSgh	CS	Glued	High	1.00	11.4	15

testing machine (1474, Zwick, Ulm) and a 1 kN load cell. In all tests, a spherical joint was used to prevent shear forces. A detailed description of the testing procedure can be found in Ref. [37]. Briefly, for diametral tensile strength tests, a piece of paper was inserted between the specimen (diameter: 10 mm; height: 5 mm) and load application surface to prevent local effects. These cylinders were tested quasi-statically at a crosshead speed of 10 mm min^{-1} . Diametral tensile strength was determined by the equation: $\frac{2F}{\pi \phi h}$. Diametral tensile strength cylinders were printed with their symmetry axis in the powder bed surface and the testing force was applied perpendicular to the printed layers. For compression strength testing, the cylinders (diameter: 5 mm; height: 10 mm), were tested quasi-statically at a crosshead speed of 1 mm min^{-1} . Compression cylinders were printed with the symmetry axis rectangular to the powder bed surface.

The mechanical properties of the green specimen (no post-processing, right after 3DP) were compared to those post-hardened in 10% phosphoric acid. Two post-hardening approaches were used according to a published method [38]. While for full dip the printed sample was fully immersed in the phosphoric acid, the samples used for partial dip only touched the surface of the phosphoric acid with the bottom of the scaffold, relying on capillary forces to soak up the solution and wet the entire sample (Fig. S3). The time for wetting the cylinders was ~ 5 s for both dipping methods.

Finally compression strength testing of the printed scaffolds was determined and compared to the compression strength of printed bulk cylinders with equivalent outer diameter. The same test setup and parameters were used as described above except for using three specimens per group.

2.3.3. Micro-computed tomography (μ CT)

The depowdering efficiency was analyzed from micro-computed tomography (μ CT40, Scanco, Switzerland) scans of printed and depowdered samples. An isotropic resolution with a voxel size of $15 \mu\text{m}$ (high resolution mode) was used. μ CT specific measurement parameters were set as follows: energy of 55 kVp, intensity of 145 μA , integration time of 200 ms and frame averaging of 3. Gaussian filtration of the scanned images was applied with a filter width 1.2 followed by global thresholding of 25% of the maximum gray scale value corresponding to a hydroxyapatite density equivalent of 393 mgHA cm^{-3} . A low degree of powder filling inside the cage, as calculated from μ CT data, was considered to be equivalent to a high depowdering efficiency.

To quantify the scaffold geometry the volume of interest defined as total volume (TV) was reduced to the inside part of the scaffold consisting of fillers only. This volume was chosen for every single scaffold and corresponded to the largest cylinder that could be fitted into the scaffold without touching the enveloping cage. All morphometric analysis was performed within this volume: bone (scaffold) volume (BV) was calculated according to literature [39]. Pore size distributions were quantified by background distance transformation [40] and visualized in histograms. Additionally trabecular (scaffold) separation (Tb.Sp) was calculated. For convenience, the bone related terms used in quantitative bone morphometry to describe microstructural properties of bone were used here to describe the scaffold geometrical properties (BV: scaffold volume; TV: total volume; Tb.Sp: separation/pore size between fillers). Selected scaffolds were visualized with cross-sectional 3D views for illustration purpose.

2.3.4. Porosity

The porosity was determined gravimetrically with the cylinders printed for mechanical testing. The density used for these calculations were based on XRD results. Theoretical densities, D_{calc} , were taken from the PDF-4+ database version 4.1102 (International Centre for Diffraction Data, ICDD, Philadelphia, USA) for α -TCP (2.863 g cm^{-3} , PDF# 04-010-4348), DCPD (2.319 g cm^{-3} , PDF# 04-013-3344) and DCP (2.922 g cm^{-3} , PDF# 04-009-3755). The porosity for the green printed specimen (before post-hardening) and for post-hardened samples were determined separately.

2.3.5. Surface analysis

Scanning electron microscopy (SEM, Zeiss EVO MA 25, Zeiss, Germany) was used to qualitatively assess the surface morphology of green (no post-hardening) and post-hardened 3DP samples. The samples were placed on a sticky carbon tape and sputtered (SCD 050 Sputter Coater, Baltec, Switzerland) with one carbon layer (two-ply carbon yarn, vacuum between 10^{-1} and 10^{-2} mbar) and then one thin gold layer (15 nm, sputter time 60 s at 40 mA).

2.4. Statistics

Statistical analysis of μ CT data was performed using a multifactorial (ANOVA) analysis to account for the effects of the different parameters (factor A: low vs. high distance between fillers, factor B: free vs. glued fillers and factor C: sandglass vs. cheese segment filler design) of interest. The significance level was set at $p < 0.01$. Further analysis of mechanical testing results was done using the open source statistics software (R 2.15.2, <http://www.r-project.org/>).

3. Results

In the pre-study, different printing parameters were varied to optimize the printing conditions. The goal was to find an optimal trade-off in printing accuracy of concave and convex design elements. Eventually, the following saturation levels and bleeding correction factors were selected: 45% and 90% saturation for the shell and the core, respectively, and bleeding correction factors of $x = 0.2$, $y = 0.2$ and $z = 0.1$ mm. Shell values were always chosen to be half of the core value to guarantee a uniform saturation of the powder with the binder.

An example of a printed benchmark and some filler specimens are shown in Fig. S4. Printing and depowdering of concave design elements such as the holes in the benchmark plate proved to be critical for powder-based 3DP. Small and deep holes could not be depowdered at all due to wicking effects (i.e. diffusion of the binder from the printed hole walls into the holes). The selection of adequate bleeding correction factors could partly reduce this problem. Interestingly, capillary effects appeared to be larger in the printing plane (x and y) than out of plane (z), so the bleeding correction factors were selected to be twice as large in the printing plane than in the z direction.

In contrast to the critical concave design elements it was shown to be by far easier to build up small fillers with mostly convex design elements (Fig. S4). A scaffold, however, requires by definition a porous volume usually realized predominantly with concave design elements such as a network of holes and pores. These conflicting requirements lead us to design a scaffold consisting of easily printable and depowderable mostly convex fillers caught in a cage with windows large enough to enable depowdering, yet small enough to prevent the fillers to leave the cage. With this new design strategy, we took advantage of the great 3DP capability of creating preassembled multiple parts within one production cycle.

Typical SEM microstructures of printed cylinders (dimension of compression samples) are illustrated in Fig. 2. Qualitative comparison of 3D printed specimens before and after post-hardening revealed that post-hardening connected the formerly loose particle network (glued together by precipitated crystals) into a much denser structure.

Weight measurement of the cylindrical samples used for the mechanical testing resulted in the porosity values shown in Table 2. For the green samples (no post-hardening) no relevant difference in porosity was found while for the post-hardened samples porosity of compression strength cylinders was 51–52% compared to 45% for the diametral tensile strength cylinders. No relevant difference for partial vs. full dip was noticed in terms of porosity.

XRD analysis revealed that after printing the degree of reaction, defined as the sum of the two reaction products DCPA (Monetite, CaHPO_4) plus DCPD (Brushite, $\text{CaHPO}_4 \cdot 2\text{H}_2\text{O}$) in wt.%, only reached $17 \pm 2\%$, leaving $83 \pm 2\%$ of unreacted α -TCP. Post-hardening by immersion of the depowdered samples in phosphoric acid increased the degree of reaction to $59 \pm 2\%$ for full dip and $57 \pm 2\%$ for partial dip. Further details can be found in Table 2.

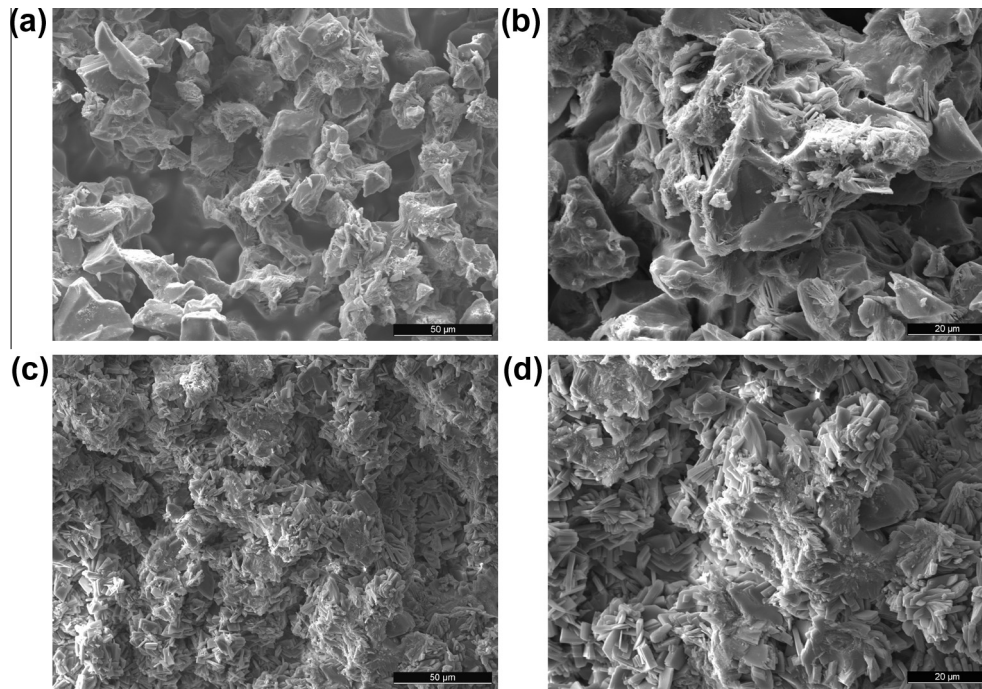


Fig. 2. Fractured surfaces after mechanical compression testing of 3DP specimen before (a and b) and after (c and d) post-hardening at two enlargements. The scale bars correspond to a size of 50 μm (a and c) and 20 μm (b and d).

Table 2

Summary of porosity, XRD and mechanical test results for green and post-hardened cylindrical samples.

		Green		Post-hardening			
		C	T	Partial dip		Full dip	
				C	T	C	T
Porosity (%)		63.4 \pm 2.5	63.5 \pm 1.0	51 \pm 2	52 \pm 3	45 \pm 1	45 \pm 1
XRD phase quantity (wt.%)	α -TCP	84 \pm 2	82 \pm 2	44 \pm 2	43 \pm 2	41 \pm 2	39 \pm 2
	Monetite	14 \pm 2	17 \pm 2	10 \pm 2	11 \pm 2	11 \pm 2	11 \pm 2
	Brushite	1 \pm 1	2 \pm 1	47 \pm 2	47 \pm 2	48 \pm 2	50 \pm 2
Mechanical properties (MPa)		1.9 \pm 0.3	0.6 \pm 0.1	8.4 \pm 3.1	7.0 \pm 1.3	1.3 \pm 0.1	1.3 \pm 0.1

C indicates samples prepared for compression strength test and T samples prepared for diametral tension strength test. Full-dip was compared to partial-dip as two different post-hardening methods.

Table 3

Dimensional accuracy of the outer diameter and the height of printed scaffolds compared to theoretical values from CAD model, together with the compressive strength of printed scaffolds and bulk cylinders with equivalent outer dimensions.

Scaff-oid	H_{CAD} (mm)	H_{3DP} (mm)	D_{CAD} (mm)	D_{3DP} (mm)	$\sigma_{C,scaf}$ (MPa)	$\sigma_{C,bulk}$ (MPa)
SGfl	11.4	11.34 \pm 0.03	14	13.85 \pm 0.12	0.38 \pm 0.08	2.66 \pm 0.37
SGfh	11.4	11.58 \pm 0.09	14.5	14.32 \pm 0.04	0.42 \pm 0.19	2.35 \pm 0.23
SGgl	11.4	11.37 \pm 0.03	14	13.76 \pm 0.05	0.61 \pm 0.28	2.66 \pm 0.37
SGgh	11.4	11.54 \pm 0.03	14.5	14.24 \pm 0.02	0.55 \pm 0.20	2.35 \pm 0.23
CSfl	11.4	11.44 \pm 0.06	15	15.03 \pm 0.28	0.74 \pm 0.16	1.91 \pm 0.23
CSfh	11.4	11.35 \pm 0.02	15	14.79 \pm 0.08	0.26 \pm 0.08	1.91 \pm 0.23
CSgl	11.4	11.42 \pm 0.03	15	14.87 \pm 0.03	1.24 \pm 0.20	1.91 \pm 0.23
CSgh	11.4	11.39 \pm 0.03	15	14.95 \pm 0.08	0.78 \pm 0.17	1.91 \pm 0.23

The compression strengths of the successfully depowdered scaffolds and the corresponding bulky cylinders are printed in bold numbers.

The results of the mechanical testing of the solid cylinders are summarized in Table 2. Compressive strength and diametral tensile testing were tested with cylindrical reference samples. Full immersion improved the compression strength values from 1.9 \pm 0.34 MPa (green body) to 6.6 \pm 1.3 MPa. Partial immersion improved the compression strength values even more reaching

8.4 \pm 3.0 MPa. Post-hardening improved diametral tensile strength from 0.6 \pm 0.1 MPa (green body) to 1.3 \pm 0.1 MPa (identical value for partial and full dip).

Additional mechanical tests yielded to compressive strengths between 0.26 and 1.24 MPa for the printed scaffolds and 1.91 to 2.35 MPa for the corresponding bulk cylinders (Table 3). Further-

more the dimensional accuracy of the printing is quantified by comparison of theoretical vs. the measured values for outer height (maximal deviation <0.2 mm) and diameter (maximal deviation <0.3 mm) of the scaffolds.

Qualitative and representative μ CT results are presented in Fig. 3. Furthermore the corresponding cumulative pore size distribution is depicted in Fig. S5. For every group of the scanned scaffolds a middle cross-section of a typical scan was chosen for illustration purposes. It is apparent that the ability to depowder a scaffold varied according to the scaffold design. For example, glued fillers appeared to be more difficult to depowder than free fillers. This impression was confirmed by the quantitative results (Fig. 4). Among all the scaffold designs, the scaffolds with free fillers and largest distance between fillers (0.5 mm for SG and 1.0 mm for CS) presented by far the lowest BV/TV values (=solid fraction; low solid fraction = good depowdering) and the highest Tb.Sp values (=mean pore size; large mean pore size = good depowdering). All other scaffold designs yielded similar results. These differences were highly significant as the effect of factor A (distance between filling objects), factor B (glued or free fillers) and factor C (sandglass vs. cheese segments), as well as the interaction between factor A and B presented a p value inferior to 0.01. In Fig. 4a) the theoretical BV/TV values based on CAD data were added for comparison with the experimental data from μ CT data. The results showed that there was an excellent match between theoretical and experimental values in two cases: SGfh and CSfh. In all other cases, the experimental values were much higher than the theoretical values.

Apart from the scaffolds presented so far, some additional scaffolds were printed for illustration purposes. Specifically, a very

small scaffold (having one glued filler only) and large scaffold (having 38 free fillers) is presented in Fig. 5. Furthermore, additional approaches suggesting possible workarounds for critical aspects of this new scaffold design are illustrated in Fig. 6 (stabilization of free fillers) and Fig. 7 (shrinking of two-part shell for void volume reduction). More details on these additional scaffolds are explained in the following discussion section.

4. Discussion

In this study the relation between scaffold design, depowdering and mechanical properties was assessed. Depowdering was investigated using microstructural morphometry. For this purpose a special focus was set on the critical inner part of the scaffold. In order to do so, the same outer cage of the scaffold was printed while the inner part was changed systematically. A factorial design of experiments was performed to assess the effect of the following three parameters on the depowdering efficiency: (i) factor A: distance between filling objects (low vs. high distance); (ii) factor B: presence of interconnections between the fillers (glued vs. free); and (iii) factor C: shape of the filling objects (sandglass vs. cheese segments). The depowdering efficiency was quantified by calculating the solid volume fraction (BV/TV) of the printed scaffolds from μ CT data.

The results revealed that depowdering was excellent provided the fillers were free to move and were not too close to each other (Fig. 4, samples SGfh & CSfh). The matching of theoretical (based on CAD models) with measured BV/TV values confirmed the excellent depowdering for these cases. This was true for both fillers, namely sandglass and cheese segments. However, while a distance of

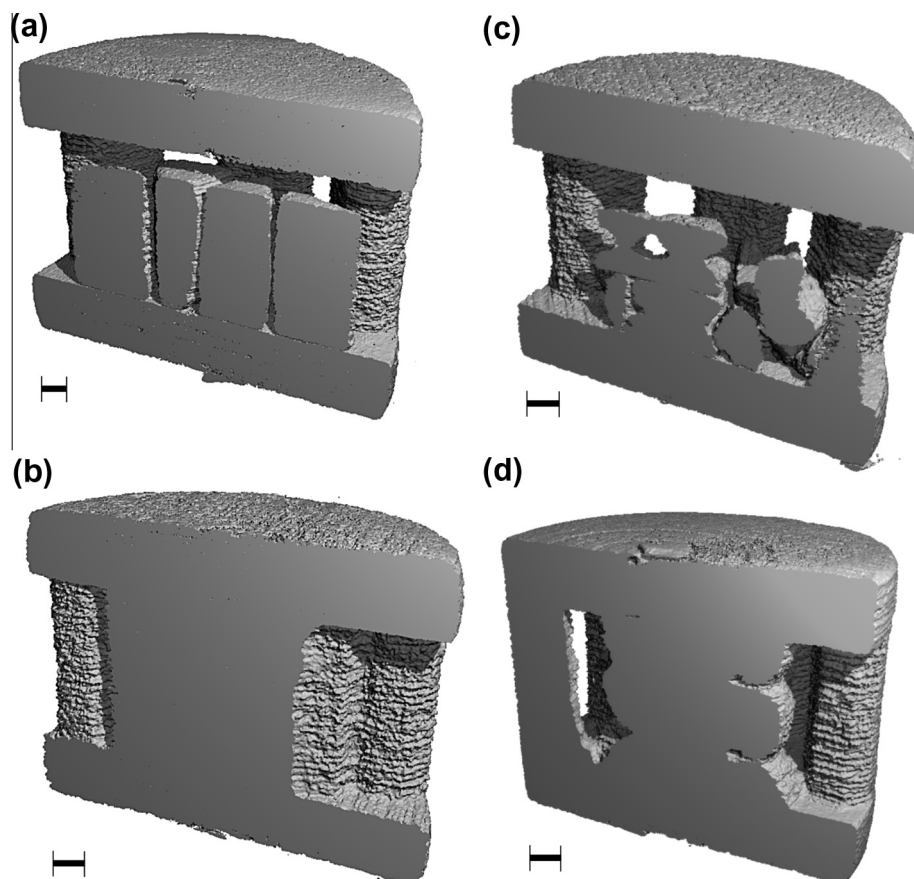


Fig. 3. μ CT scans showing cross-sections of cheese segment (CS) and sandglass (SG) scaffolds while the scale bar indicates a length of 1 mm. Fillers placed at a high distance were easily depowdered (a and c), while glued (b and d) and too close fillers (not illustrated) could not be depowdered.

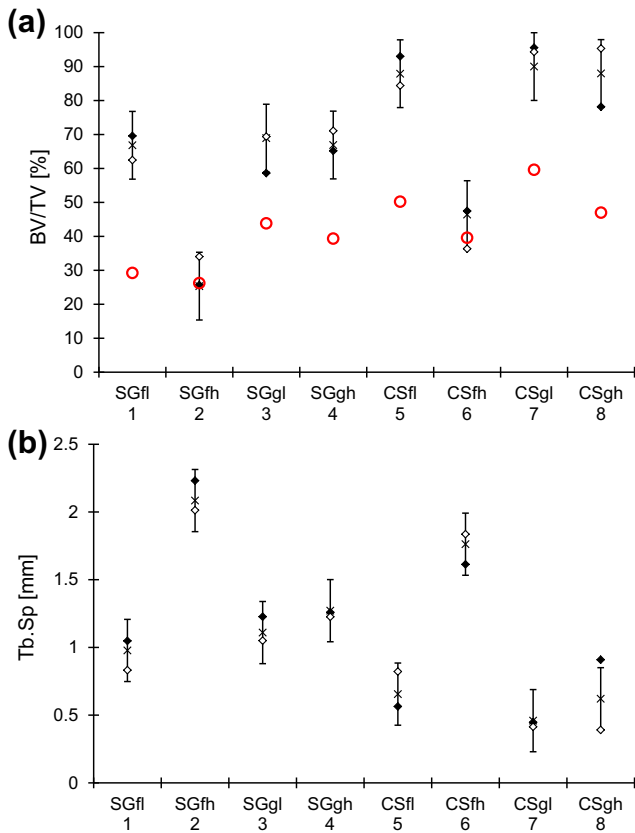


Fig. 4. Dependency of BV/TV (a) and Tb.Sp (b) on filler type (SG, CS), filler design (f: free fillers, g: glued fillers) and filler distance (l: low distance between fillers, h: high distance between fillers). The symbols (x) correspond to the adjusted values according to the statistical model. The symbols (◇ ◆) correspond to the measured data points and the error bars to the 95% confidence intervals. The symbols (○) correspond to theoretical BV/TV values. Definition of nomenclature can be found in Table 2.

0.5 mm was sufficient to enable complete depowdering of sandglasses, a distance of 1.0 mm was required for cheese segments. This was probably related to the height difference of these fillers: 2.4 mm for sandglasses and 5.4 mm for cheese segments. Indeed, as soon as the first sandglass filler was depowdered, the movement of this free filler simplified depowdering of adjacent fillers. This process was repeated until the air stream used for depowdering found its way from one window of the scaffold cage to another. At this point of time the airstream was deviated due to the presence of free fillers (and the cylindrical inside walls) leading to a vortex effect. This effect finally leads to a loosening of the inner parts that still were not depowdered completely, eventually allowing the core of the scaffold to be depowdered. This inner volume typically cannot be depowdered using a conventional rigid scaffold design. This synergetic effect between small fillers and air stream was obviously more limited with larger or glued fillers. Since this effect should not be limited by a change of scaffold volume, additional scaffolds were printed to further illustrate the advantage of this new scaffold design. First, a single sandglass filler glued into a small scaffold cage (Fig. 5a) was printed and depowdered without any difficulties (Fig. 5b). This is in contrast with the very poor depowdering noticed for the scaffolds filled with 14 glued SG fillers (Fig. 4; scaffold “SGgh”) emphasizing the strong size-dependency of the depowdering efficiency. In contrast, a much larger scaffold containing 38 SG free fillers (instead of 14 fillers in the conventional design used in this study) was printed and depowdered without difficulties (Fig. 5c and d). In other words, the depowdering advantage gained by printing free and mobile fillers in the core of the

scaffolds increases with the scaffold volume. This principle could open up the door for even larger and more complex porous scaffolds based on powder-based 3DP.

Despite the promising improvements in depowdering observed with the new cage design, some other aspects have to be considered critically. For example, while free fillers allow excellent depowdering characteristics, relative movement between fillers could affect the biological response negatively. Possible work-around procedures are post filling of the cages with blood or a highly viscous putty material such as e.g. hyaluronic acid. Alternatively, full and even partial dip of a scaffold with free sandglass structures in 10% phosphoric acid was effective not only concerning mechanical properties of the cage (Table 2) but also for gluing the fillers together (Fig. 6). Another limitation of the present design strategy is related to the fact that the free fillers drop down to the bottom of the scaffold cage after depowdering. While this “dropping-effect” is large with small fillers it is smaller with large fillers (cheese segments). On the other side these larger fillers reduce the porosity, since large volumes inside the scaffold cage are filled out already. In this study only two filler designs were studied. A systematic optimization of filler design and desired morphometric parameters will be necessary for a better understanding of these relations. With an optimized design of fillers even a nearer distance could be feasible, allowing even higher filling degree of the inside part of the scaffold volume while still maintaining a controlled interconnected porosity. Ideally, the entire inner volume would be filled with fillers interlocking to its neighbors after depowdering and thus preventing any relative motion. Alternatively, novel design approaches could be explored. For example, shrinkable scaffolds with interlocking interfaces could enable an inner volume reduction after depowdering (Fig. 7). After depowdering and breaking up of predetermined breaking points, the void volume in the center could be reduced as desired. Again a post-hardening step could be applied for stabilization of scaffold cage and fillers. Even though the feasibility of this principle was demonstrated here, in depth optimization of such approaches is beyond the scope of this study.

In summary, the new printing design with free fillers allowed the synthesis of fully depowdered scaffolds. The mechanical stability of the green body was high enough to prevent the mechanical failure of the free fillers during depowdering and the scaffold in general. However the compression strength of the successfully depowdered scaffolds (Table 3, bold numbers) only reached 14–18% of the values measured for the equivalent bulky cylinders. On one hand this indicates the limitation of the current design approach. On the other hand the aim of this study was focused on design aspects. To improve mechanical properties, two approaches are envisioned. Design optimization of the cage geometry could be an interesting starting point for future studies. In this study, another material-based approach elucidated the feasibility of higher mechanical properties by post-hardening of printed samples in phosphoric acid. A thorough analysis of the mechanical properties, porosities and XRD results allowed a better understanding of the interplay between these properties. Generally, a more complete post-hardening decreases the porosity and the α -TCP content, and increases the mechanical properties (Table 2). The difference of porosity results between compression cylinders and tension cylinders is probably related to a difference in volume and drying time. During post-hardening the compression cylinders, having smaller volumes, dried faster than the tension cylinders with larger volumes. This lead to a higher dilution and finally lower total porosity of the large diametral tensile strength samples. XRD results revealed that in our study only a small portion of the α -TCP powder (<20 wt.%) reacted into brushite and monetite. Only <2 wt.% reacted into brushite phase, explaining the low mechanical integrity of the printed green parts. Precipitated brushite crystals

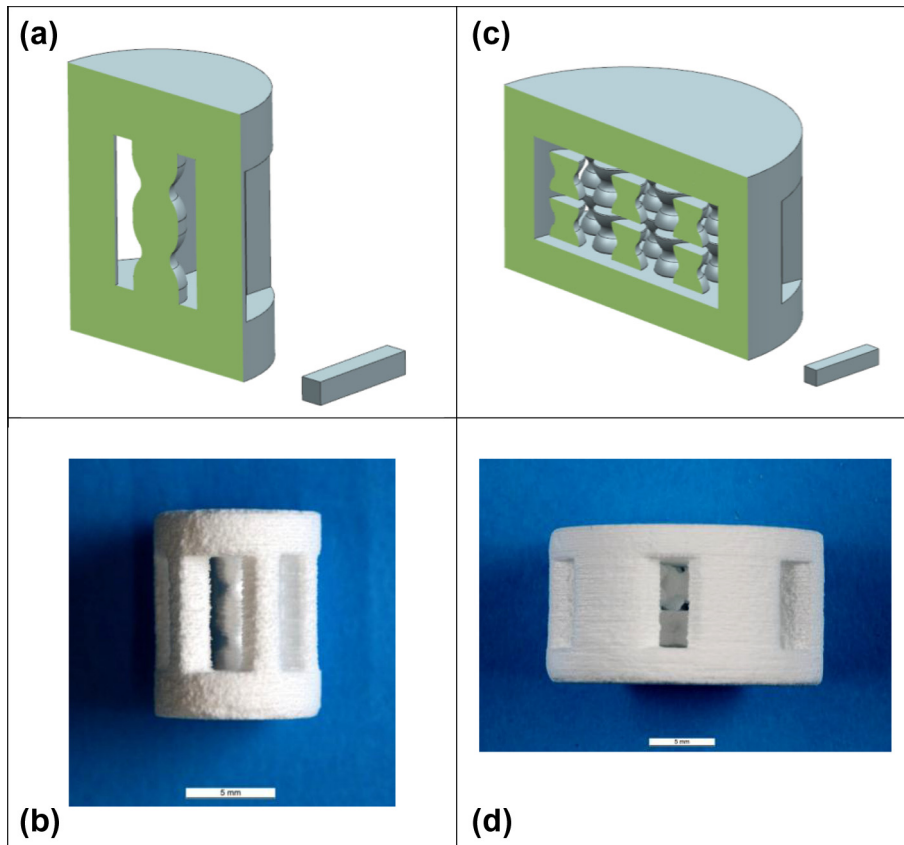


Fig. 5. CAD models (a and c) and 3D printed specimen (b and d) of a small SG scaffold (a and b) and a large sandglass scaffold with 38 fillers (c and d). The bar corresponds to a length of 5 mm.

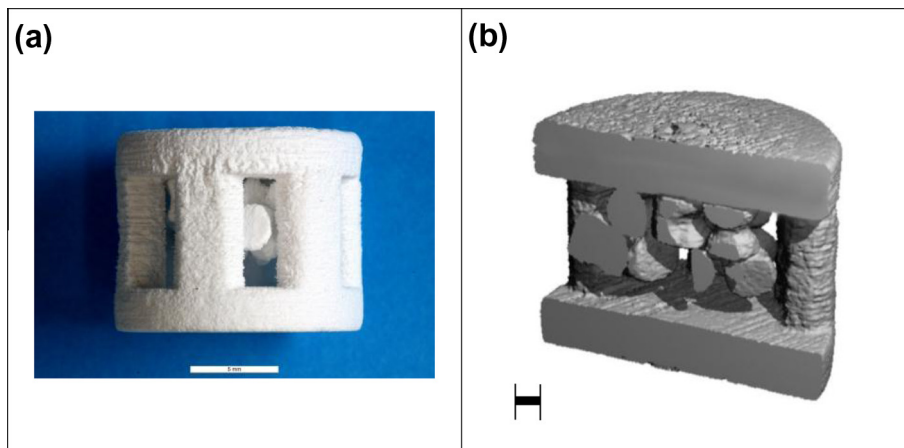


Fig. 6. Photo (a) and μ CT scan (b) of a 3D printed SG specimen with free fillers. The free fillers are stabilized by partial dip of the scaffold in phosphoric acid. The scaffold is recorded upside down, demonstrating the stabilized fillers glued to bottom. The scale bar of the μ CT scan indicates a length of 1 mm while the bar in the image corresponds to a length of 5 mm.

often develop large crystals enhancing mechanical entanglement resulting in higher strength cements than smaller and less entangled monetite crystals [41]. After post-hardening the amount of brushite was increased up to 50 wt.%. This effect was also nicely confirmed by the SEM images, showing the formation of idiomorphic crystals on the surface of initial powder particles (Fig. 2). No relevant differences were detected between full and partial dip.

Mechanical testing of 3D printed cylinders revealed the necessity for post-hardening steps after 3DP. The initial (green) mechan-

ical integrity just after 3DP was found to be very low for the small bulk cylinders tested (strength <2 MPa) and even lower for the printed scaffolds (strength <1.3 MPa). This is critical for the depowdering step, since post-hardening is possible after depowdering only and therefore fine structures can easily be destroyed by the actual depowdering process. Post-hardening of printed cylinders lead to more than three to four times higher compression strength, resulting in a range suggested for cancellous bone scaffolds [42]. The increase in mechanical stability is probably related to the glu-

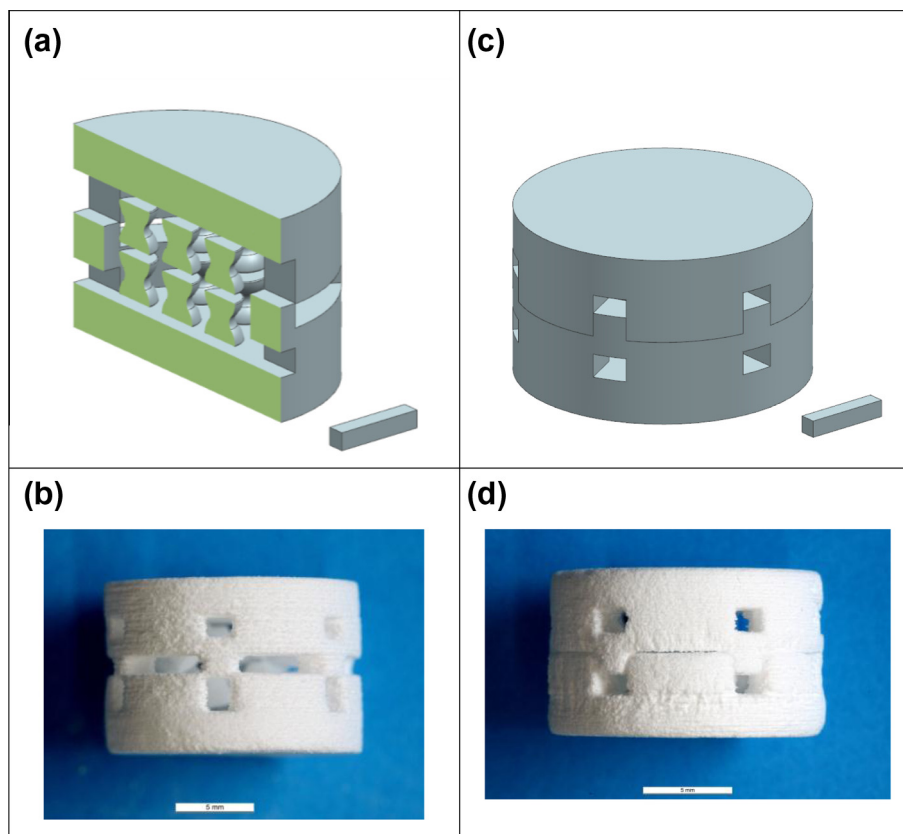


Fig. 7. Example of a shrinkable scaffold CAD model (a and c) and 3D printed specimen (b and d). The two main stages consist of the scaffold just after 3D printing before compaction (left column) vs. the scaffolds after compaction (right column). Pressing together the two parts of the cage (a and b) allows a reduction of the gap between fillers and cage (c and d), and thus a better control of the dropping effect. If required, the compacted scaffold can also be post-hardened for joining the two part cage and stabilization of the fillers. The bar corresponds to a length of 5 mm.

ing effect of entangled brushite and monetite crystals. In the literature, even greater rise (up to >40 MPa) due to post-hardening and sintering could be achieved [37]. Full-dip post-hardening led to lower compression strength compared to partial-dip. Even though these changes were not significant, a clear tendency was observed. The results, however, clearly indicated the benefit of partial-dip compared to full-dip. This is in agreement with published results showing that partial dipping led to a more thorough impregnation than full dipping [38]. This effect is related to capillary effects and air bubbles trapped inside pores preventing or limiting wetting.

5. Conclusion and outlook

This study analyzed the relations between different scaffold designs and depowdering efficiency by using μ CT to quantify morphometric structural indices. Furthermore the mechanical properties and the effect of different post-hardening methods for bulk specimens were analyzed.

The study revealed that depowdering, especially of the scaffold center, was significantly improved when the filling objects were free to move and not placed too close to each other. The free movement of the outer fillers at the periphery helped to clear the remaining powder of the very inner part of the scaffold. The minimal distance allowing the fillers to be freed to move was 1 mm for large filler objects such as the cheese segments, while for the smaller objects such as sandglass fillers a distance of 0.5 mm was sufficient. Generally, depowdering was found to be uncritical for small scaffolds (single glued filler). However, it became critical when the fillers were glued in position. When the fillers were free

to move, a synergetic effect between free filler motion and compressed air could be achieved, leading to clear depowdering benefits. As a result, it was possible to print large scaffolds. In fact, the results suggest that an increase of scaffold size does not worsen depowdering, in contrast to what is observed with traditional (rigid) scaffold designs. In light of these insights this new depowdering-friendly design could open new doors for the 3DP synthesis of tissue engineering scaffolds and bone substitutes.

Acknowledgements

Funding from RMS Foundation is gratefully acknowledged. The authors express their appreciation to G. Bigolin and O. Loeffel from the RMS Foundation for support in mechanical testing and SEM analysis.

Appendix A. Figures with essential colour discrimination

Certain figures in this article, particularly Figs. 1 and 4–7 are difficult to interpret in black and white. The full colour images can be found in the on-line version, at <http://dx.doi.org/10.1016/j.actbio.2013.07.019>.

Appendix B. Supplementary data

Supplementary data associated with this article can be found, in the online version, at <http://dx.doi.org/10.1016/j.actbio.2013.07.019>.

References

- [1] Butscher A, Bohner M, Hofmann S, Gauckler L, Muller R. Structural and material approaches to bone tissue engineering in powder-based three-dimensional printing. *Acta Biomater* 2011;7:907–20.
- [2] Constantz BR, Ison IC, Fulmer MT, Poser RD, Smith ST, VanWagoner M, et al. Skeletal repair by in situ formation of the mineral phase of bone. *Science* 1995;267:1796–9.
- [3] Bohner M. Calcium orthophosphates in medicine: from ceramics to calcium phosphate cements. *Injury* 2000;31(Suppl. 4):37–47.
- [4] Moseke C, Gbureck U. Tetracalcium phosphate: synthesis, properties and biomedical applications. *Acta Biomater* 2010;6:3815–23.
- [5] Bose S, Tarafder S. Calcium phosphate ceramic systems in growth factor and drug delivery for bone tissue engineering: a review. *Acta Biomater* 2012;8.
- [6] LeGeros RZ. Properties of osteoconductive biomaterials: calcium phosphates. *Clin Orthop Relat Res* 2002;81–98.
- [7] Dorozhkin SV. Bioceramics of calcium orthophosphates. *Biomaterials* 2010;31:1465–85.
- [8] Habibovic P, Gbureck U, Doillon CJ, Bassetta DC, van Blitterswijk CA, Barralet JE. Osteoconduction and osteoinduction of low-temperature 3D printed bioceramic implants. *Biomaterials* 2008;29:944–53.
- [9] Tamimi F, Torres J, Gbureck U, Lopez-Cabarcos E, Bassett DC, Alkhraisat MH, et al. Craniofacial vertical bone augmentation: a comparison between 3D printed monolithic monetite blocks and autologous on lay grafts in the rabbit. *Biomaterials* 2009;30:6318–26.
- [10] Becker ST, Bolte H, Krapf O, Seitz H, Douglas T, Sivananthan S, et al. Endocultivation: 3D printed customized porous scaffolds for heterotopic bone induction. *Oral Oncol* 2009;45:E181–8.
- [11] Merten HA, Wiltfang J, Grohmann U, Hoening JF. Intra-individual comparative animal study of alpha- and beta-tricalcium phosphate degradation in conjunction with simultaneous insertion of dental implants. *J Craniofac Surg* 2001;12:59–68.
- [12] Fierz FC, Beckmann F, Huser M, Irsen SH, Leukers B, Witte F, et al. The morphology of anisotropic 3D-printed hydroxyapatite scaffolds. *Biomaterials* 2008;29:3799–806.
- [13] Khalyfa A, Vogt S, Weisser J, Grimm G, Rechtenbach A, Meyer W, et al. Development of a new calcium phosphate powder-binder system for the 3D printing of patient specific implants. *J Mater Sci Mater Med* 2007;18:909–16.
- [14] Vorndran E, Klarner M, Klammert U, Grover LM, Patel S, Barralet JE, et al. 3D powder printing of beta-tricalcium phosphate ceramics using different strategies. *Adv Eng Mater* 2008;10:B67–71.
- [15] Fielding GA, Bandyopadhyay A, Bose S. Effects of silica and zinc oxide doping on mechanical and biological properties of 3D printed tricalcium phosphate tissue engineering scaffolds. *Dent Mater* 2012;28.
- [16] Gildenhaar R, Knabe C, Gomes C, Linow U, Houshmand A, Berger G. Calcium alkaline phosphate scaffolds for bone regeneration 3Dfabricated by additive manufacturing. *Key Eng Mater* 2012;1:849–54.
- [17] Tarafder S, Balla VK, Davies NM, Bandyopadhyay A, Bose S. Microwave-sintered 3D printed tricalcium phosphate scaffolds for bone tissue engineering. *J Tissue Eng Regen Med* 2013;7(8):631–41.
- [18] Winkel A, Meszaros R, Reinsch S, Mueller R, Travitzky N, Fey T, et al. Sintering of 3D-printed glass/HAp composites. *J Am Ceram Soc* 2012;95:3387–93.
- [19] Peters F, Groisman D, Davids R, Hanel T, Durr H, Klein M. Comparative Study of patient individual implants from beta-tricalcium phosphate made by different techniques based on CT data. *Materialwiss Werkst* 2006;37:457–61.
- [20] Hänel T, Peters F, Ch. H, Dürr H. Aus CT-Daten generierte patientenindividuelle Implantate aus β -Tricalciumphosphat für die Knochenregeneration. *Z Reg Med* 2009;2:13–7.
- [21] Butscher A, Bohner M, Doebelin N, Galea L, Loeffel O, Müller R. Moisture based three-dimensional printing of calcium phosphate structures for scaffold engineering. *Acta Biomater* 2013;9:5369–78.
- [22] Bohner M, Loosli Y, Baroud G. Commentary: deciphering the link between architecture and biological response of a bone graft substitute. *Acta Biomater* 2011;7:478–84.
- [23] Karageorgiou V, Kaplan D. Porosity of 3D biomaterial scaffolds and osteogenesis. *Biomaterials* 2005;26:5474–91.
- [24] Bohner M, van Lenthe GH, Grunenfelder S, Hirsiger W, Evison R, Muller R. Synthesis and characterization of porous beta-tricalcium phosphate blocks. *Biomaterials* 2005;26:6099–105.
- [25] Butscher A, Bohner M, Roth C, Ernstberger A, Heuberger R, Doebelin N, et al. Printability of calcium phosphate powders for three-dimensional printing of tissue engineering scaffolds. *Acta Biomater* 2012;8:373–85.
- [26] Gbureck U, Holzel T, Doillon CJ, Muller FA, Barralet JE. Direct printing of bioceramic implants with spatially localized angiogenic factors. *Adv Mater* 2007;19:795–800.
- [27] Tamimi F, Sheikh Z, Barralet J. Dicalcium phosphate cements: brushite and monetite. *Acta Biomater* 2012;8:474–87.
- [28] Tamimi F, Torres J, Bassett D, Barralet J, Cabarcos EL. Resorption of monetite granules in alveolar bone defects in human patients. *Biomaterials* 2009;31:2762–9.
- [29] Theiss F, Apelt D, Brand D, Bohner M, Frei C, Zlinsky K, et al. Biocompatibility and resorption of a new brushite calcium phosphate cement. Prague: ECVS; 2004. p. 143–6.
- [30] Arora R, Milz S, Sprecher C, Sitte I, Blauth M, Lutz M. Behaviour of ChronOS™ Inject in metaphyseal bone defects of distal radius fractures: tissue reaction after 6–15 months. *Injury* 2012;43:1683–8.
- [31] Klammert U, Reuther T, Jahn C, Kraski B, Kubler AC, Gbureck U. Cytocompatibility of brushite and monetite cell culture scaffolds made by three-dimensional powder printing. *Acta Biomater* 2009;5:727–34.
- [32] Habibovic P, de Groot K. Osteoinductive biomaterials – properties and relevance in bone repair. *J Tissue Eng Reg Med* 2007;1:25–32.
- [33] Taut T, Kleeberg R, Bergmann J. The new Seifert Rietveld program BGMN and its application to quantitative phase analysis. *Mater Struct* 1998;5:57–66.
- [34] Mathew M, Schroeder LW, Dickens B, Brown WE. The crystal structure of $[\alpha]\text{-Ca}_3(\text{PO}_4)_2$. *Acta Crystallogr B* 1977;33:1325–33.
- [35] Dickens B, Bowen JS, Brown WE. A refinement of the crystal structure of CaHPO_4 (synthetic monetite). *Acta Crystallogr* 1971;B28:797–806.
- [36] Curry NA, Jones DW. Crystal structure of brushite, calcium hydrogen orthophosphate dihydrate: a neutron-diffraction investigation. *J Chem Soc A* 1971:3725–9.
- [37] Gbureck U, Hoelzel T, Biermann I, Barralet JE, Grover LM. Preparation of tricalcium phosphate/calcium pyrophosphate structures via rapid prototyping. *J Mater Sci Mater Med* 2008;19:1559–63.
- [38] Stahli C, Bohner M, Bashoor-Zadeh M, Doebelin N, Baroud G. Aqueous impregnation of porous beta-tricalcium phosphate scaffolds. *Acta Biomater* 2010;6:2760–72.
- [39] Hildebrand T, Laib A, Muller R, Dequeker J, Ruegsegger P. Direct three-dimensional morphometric analysis of human cancellous bone: microstructural data from spine, femur, iliac crest, and calcaneus. *J Bone Miner Res* 1999;14.
- [40] Hildebrand T, Ruegsegger P. A new method for the model-independent assessment of thickness in three-dimensional images. *J Microsc (Oxford)* 1997;185:67–75.
- [41] Hofmann MP, Mohammed AR, Perrie Y, Gbureck U, Barralet JE. High-strength resorbable brushite bone cement with controlled drug-releasing capabilities. *Acta Biomater* 2009;5:43–9.
- [42] Bose S, Roy M, Bandyopadhyay A. Recent advances in bone tissue engineering scaffolds. *Trends Biotechnol* 2012;30.